



# Study of hydraulic fracture growth behavior in heterogeneous tight sandstone formations using CT scanning and acoustic emission monitoring

Nai-Zhen Liu<sup>1</sup> · Yu-Shi Zou<sup>2</sup> · Xin-Fang Ma<sup>2</sup> · Ning Li<sup>2</sup> · Shan Wu<sup>2</sup>

Received: 14 March 2018 / Published online: 13 December 2018  
© The Author(s) 2018

## Abstract

Tortuous hydraulic fractures (HFs) are likely to be created in heterogeneous formations such as conglomerates, which may cause sand plugging, ultimately resulting in poor stimulation efficiency. This study aims to explore HF growth behavior in conglomerate through laboratory fracturing experiments under true tri-axial stresses combined with computed tomography scanning and acoustic emission (AE) monitoring. The effects of gravel size, horizontal differential stress, and AE focal mechanisms were examined. Especially, the injection pressure and the AE response features during HF initiation and propagation in conglomerate were analyzed. Simple HFs with narrow microfractures are created in conglomerate when the gravels are considerably smaller than the specimen, whereas complex fractures are created when the gravels are similar in size to the specimen, even under high horizontal differential stresses. Breakdown pressure and AE rates are high when a HF is initiated from the high-strength gravel. A large pressure decline after the breakdown may indicate the creation of a planar and wide HF. Analyzing the focal mechanism indicates that the shear mechanism generally dominates with an increase in the HF complexity. Tensile events are likely to occur during HF initiation and are located around the wellbore. Shear events occur mainly around the nonplanar and complex matrix/gravel interfaces.

**Keywords** Conglomerate · Gravel · Hydraulic fracturing · Propagation mechanism · Computed tomography (CT) · Acoustic emission (AE)

## 1 Introduction

Hydraulic fracturing is an essential technology for hydrocarbon development in a conglomerate reservoir with low or ultra-low porosity and permeability. The resulting hydraulic fractures (HFs) during a fracturing treatment are expected to be filled adequately with proppant to provide sufficient conductivity for hydrocarbon flow (Hu et al. 2018a, b; Tang et al. 2018a, b). However, the stimulation efficiency is generally poor owing to the poor reservoir features, such as large variability of lithology and strong

heterogeneity in conglomerate reservoirs. Gravel particles may cause extreme tortuosity and complexity of HFs, which could impede proppant transport inside HFs. Therefore, a thorough understanding of the propagation behavior of HF in conglomerate reservoirs is significant from the viewpoint of an effective fracture design.

In conglomerate, complex growth behavior of a HF is mainly attributed to the significant difference in the mechanical properties between the rock matrix and gravel particles (Ma et al. 2017). Four types of HF intersections with gravel particles have been reported in the literature, namely penetration, deflection, termination, and attraction (Meng et al. 2010; Li et al. 2013; Ju et al. 2016a, b; Ma et al. 2017). The interaction behavior depends closely on the horizontal differential stress, gravel properties (e.g., size, volume content, and mechanical properties), injection rate, and fluid viscosity. HF tends to penetrate the gravel particles under a high horizontal differential stress when a highly viscous fluid is used, whereas HF tends to be deflected to the matrix/gravel interfaces under a low

Edited by Yan-Hua Sun

✉ Yu-Shi Zou  
zouyushi@126.com

<sup>1</sup> CNPC Great Wall Drilling Company, Beijing 100101, China

<sup>2</sup> State Key Laboratory of Petroleum Resources and Prospecting, China University of Petroleum, Beijing 102249, China

horizontal differential stress when a low viscosity fluid is used (Meng et al. 2010; Li et al. 2013; Ju et al. 2016a, b; Ma et al. 2017). However, nearly all of these studies used artificial specimens and numerical models to investigate the HF growth behavior in conglomerate formations. These artificial and numerical specimens cannot represent natural conglomerates because of significant differences in rock mechanical properties. This phenomenon may limit laboratory studies from producing representative test results, and the results obtained in this manner would be unsuitable for extrapolation to field conditions. Therefore, laboratory experiments on real conglomerate specimens are necessary for investigating the influence of gravels on HF growth geometry.

Acoustic emission (AE) has been an effective technique for monitoring HFs in laboratory experiments, and it is recognized as a high-frequency analog of induced microseismicity in the field (Mogi 1967; Lockner and Byerlee 1977; Zoback et al. 1977; Talebi and Cornet 1987; Stanchits et al. 2006, 2012, 2015; Frash et al. 2013; Hampton et al. 2013; Yashwanth et al. 2013; Li et al. 2018a). A precise technique, namely high-resolution industrial computed tomography (CT) scanning, has been used increasingly to describe the complex HF geometry created in rocks with lithological heterogeneity and anisotropy (Ju et al. 2016a, b; Zou et al. 2016, 2017; Ma et al. 2017). However, information about the relationship between HF growth behavior and AE response feature in conglomerate remains scarce, thus possibly limiting the interpretation of

microseismic data of fracturing processes in conglomerate reservoirs. The combined use of CT scanning and AE monitoring in the laboratory can help with accurately understanding HF growth behavior in conglomerate formations.

In the present study, laboratory fracturing tests were conducted on natural conglomerate specimens (30 cm × 30 cm × 30 cm) by using a true tri-axial fracturing system. Specifically, we reported the results of CT scanning and AE monitoring images of HFs in conglomerates with different gravel sizes and horizontal differential stresses. In addition, the features of the injection pressure curve and the AE focal mechanism were also analyzed to further illustrate the HF growth behavior in conglomerate formations.

## 2 Experimental methods

### 2.1 Specimen descriptions

Four cubic conglomerate specimens of 30 cm × 30 cm were prepared for fracturing experiments. A central hole with 1.6 cm diameter and 16.5 cm depth was drilled into the specimens to model the wellbore. Then, a 13.5-cm-long steel tube with internal and external diameters of 0.8 and 1.5 cm, respectively, was bonded to the hole using high-strength epoxy glue. Ultimately, a 3-cm-long open hole was left to be pressurized by pumping the

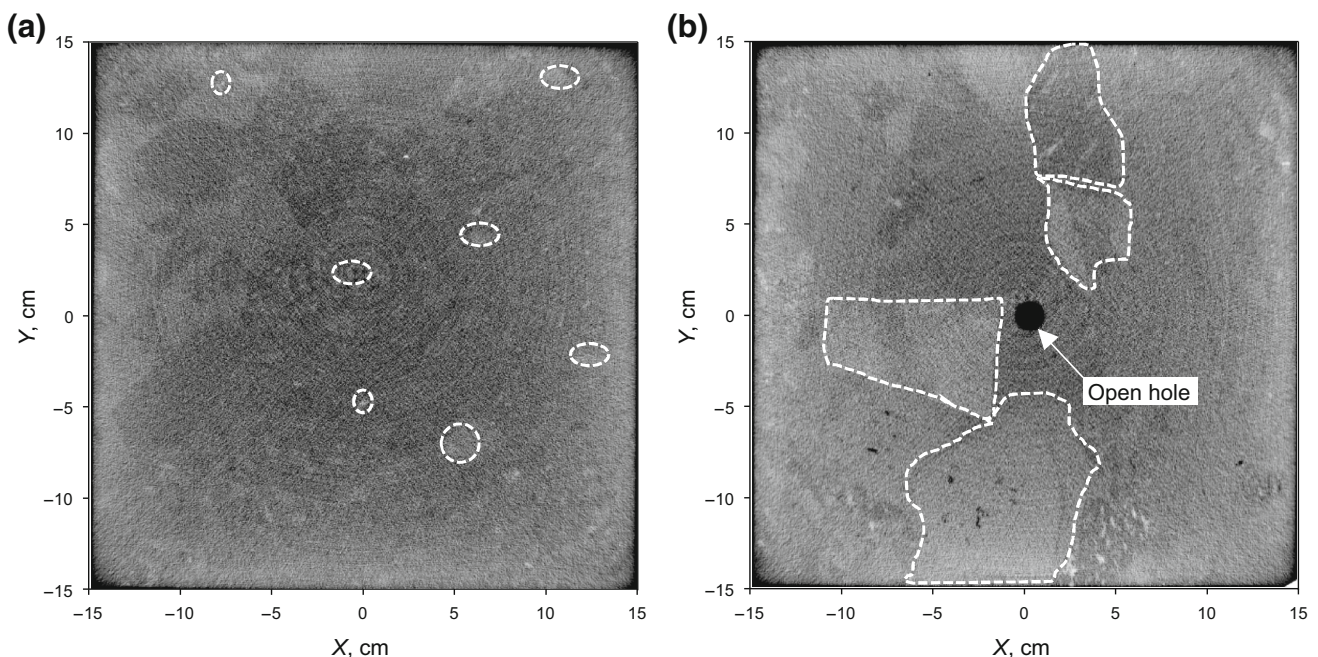


**Fig. 1** Gravel (enclosed by white dotted lines) distributions in conglomerate specimens determined by CT scanning. **a** Small gravels with favorable sorting. **b** Large gravels with poor sorting (after Ma et al. 2017)

**Table 1** Statistical characteristics of gravel sizes in conglomerate specimens

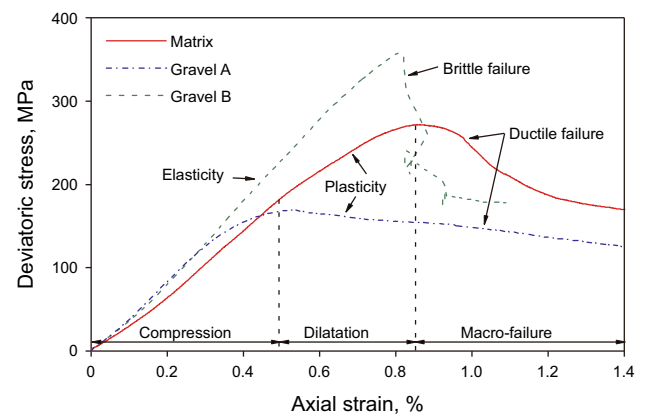
Specimen no.	Main gravel size, mm	Max gravel size, mm	Grain sorting
1	2–15	20	Good
2	5–20	50	Good
3	5–100	163	Poor
4	5–80	112	Poor

**Table 2** Mineral composition from X-ray diffraction and mechanical parameters

	Mineral composition, %					Poisson's ratio	Young's modulus, GPa	Tensile strength, MPa	Compressive strength, MPa
	Quartz	Carbonate	Clay	Feldspar	Others				
Matrix	20.8	19.0	16.3	39.4	4.5	0.25	36.7	8.1	246.8
Gravel-A	23.8	10.9	5.3	55.4	4.6	0.27	45.7	4.1	169.2
Gravel-B	81.5	11.4	1.2	–	5.9	0.25	50.1	12.4	358.1
<i>Interfaces</i>									
Matrix/gravel-A	–	–	–	–	–	–	–	4.3	–
Matrix/gravel-B	–	–	–	–	–	–	–	7.4	–

fracturing fluid into the wellbore. The conglomerate specimens were highly heterogeneous because of numerous gravel particles of various sizes. The gravel particle distributions within the specimens can be observed using a high energy industrial CT scanning system with a maximum ray source voltage of 450 kV, spatial resolution of 2 lp/mm, and density resolution of 0.4% (Zou et al. 2016, 2017; Ma et al. 2017), as illustrated in Fig. 1. Specimens 1 and 2 show similar gravel sizes and contain numerous relatively small gravel particles (considerably smaller in size than the specimens) with favorable sorting, whereas Specimens 3 and 4 contain numerous relatively large gravel particles (of sizes similar to the specimen size) with poor sorting (Table 1). The mineral compositions and mechanical parameters of the matrix and various gravel particles differ significantly. Two types of gravel particles with different lithologies and mechanical properties were observed in the conglomerate specimens. The first and second types of gravel particles (Gravels A and B, respectively) contained high amounts of feldspar and quartz, respectively. Table 2 summarizes the mineral composition and the mechanical parameters determined by X-ray diffraction, Brazilian splitting, and triaxial compression (Ma et al. 2017).

In the tri-axial compression tests, the cylindrical specimens used herein (2.5 cm in diameter and 5 cm in length) were drilled from the matrix and the two types of intact gravel particles considered in the present study. Figures 2 and 3 depict the obviously different stress–strain curves and the failure surface morphologies created. For the matrix specimen, the nonlinear stress–strain curve was

**Fig. 2** Stress–strain curves of conglomerate specimens

presented during the early loading stage (Fig. 2, red curve). This phenomenon may be ascribed to the compression of microfractures that existed initially in the matrix along with numerous small gravel particles. In the pre-peak stage, the reducing slope of the stress–strain curve indicated dilatation of the microfractures in the matrix specimen. The matrix specimen still can maintain some residual strength to support the load, although this matrix specimen failed macroscopically under a deviatoric stress of 246.8 MPa. The matrix specimen presented a plastic deformation feature. In this case, the fracture extended tortuously along the matrix/gravel interfaces, as displayed in Fig. 3a. For the intact gravel specimens (Gravels A and B), the linear stress–strain curve was presented in the early loading stage. However, significant differences appeared after the linear elasticity part. Gravel-A with 55.4% feldspar underwent

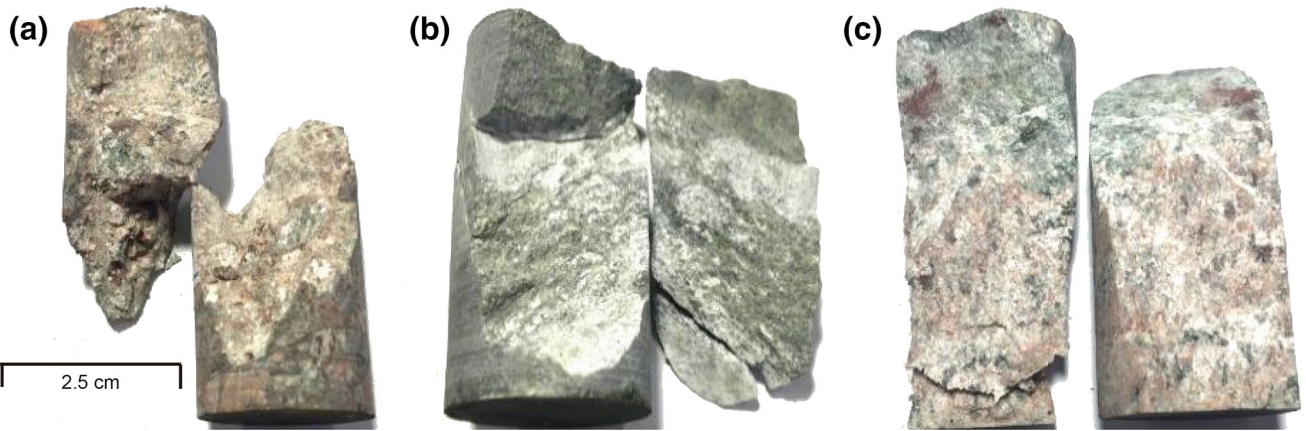


Fig. 3 Cylindrical conglomerate specimens (2.5 cm in diameter, 5 cm in length) after triaxial compression tests

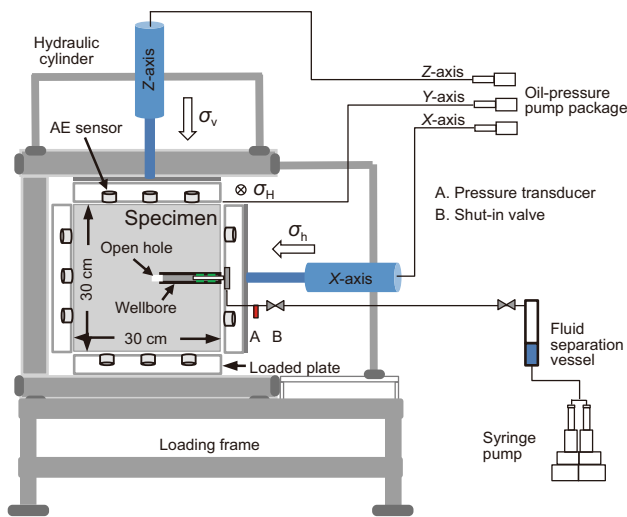


Fig. 4 Cross-sectional view of the experimental setup used for fracturing experiments

plastic deformation and fractured under a low deviatoric stress of 169.2 MPa (Fig. 2, blue curve), whereas Gravel-B with 81.5% of quartz mainly experienced elastic deformation and fractured under the highest deviatoric stress of 358.1 MPa (Fig. 2, green curve). This phenomenon indicates that brittle failure tends to occur when quartz dominates the mineral composition. Figure 3b, c presents more

planar fracture surfaces obtained in the intact gravels than those created in the matrix (Fig. 3a).

### 2.2 Experimental procedure

Fracturing experiments were conducted using a true triaxial hydraulic fracturing system (Ma et al. 2017; Zou et al. 2017), as demonstrated in Fig. 4. The wellbore inside the specimen was set horizontally and parallel to the X-axis. The AE sensors were fitted inside the loaded plates and placed in direct contact with the specimen surfaces. Furthermore, 16 AE sensors were connected to a data acquisition system. A continuous collection mode was set to monitor the AE activity during the experiment. Stresses were applied to the specimen independently along the X-, Y-, and Z-axes in the Cartesian coordinate system using an oil pressure pump package. Vertical stress ( $\sigma_v$ ) was applied in the Z-axis; the minimum ( $\sigma_h$ ) and maximum ( $\sigma_H$ ) horizontal stresses were applied along the X- and Y-axes, respectively.

Cross-linked gel with a viscosity of  $\mu = 120$  mPa s, mixed with a red tracer, was poured directly into a fluid separation vessel. Then, the fracturing fluid was discharged from the vessel into the wellbore using a syringe pump to initiate HF from the open hole. Fluid injection was performed at a constant rate of  $Q = 20$  mL/min for approximately 600 s, after which the syringe pump was shut down. The injection pressure at the well head was monitored during this process. The AE sensors in contact with the specimen surface could alternately receive a waveform.

Table 3 Parameters used in fracturing experiments

Specimen no.	$\sigma_v$ , MPa	$\sigma_h$ , MPa	$\sigma_H$ , MPa	$\sigma_H - \sigma_h$ , MPa	$\mu$ , mPa s	$Q$ , mL/min
1	20	5	15	10	120	20
2	20	5	5	0	120	20
3	20	5	15	10	120	20
4	20	5	5	0	120	20

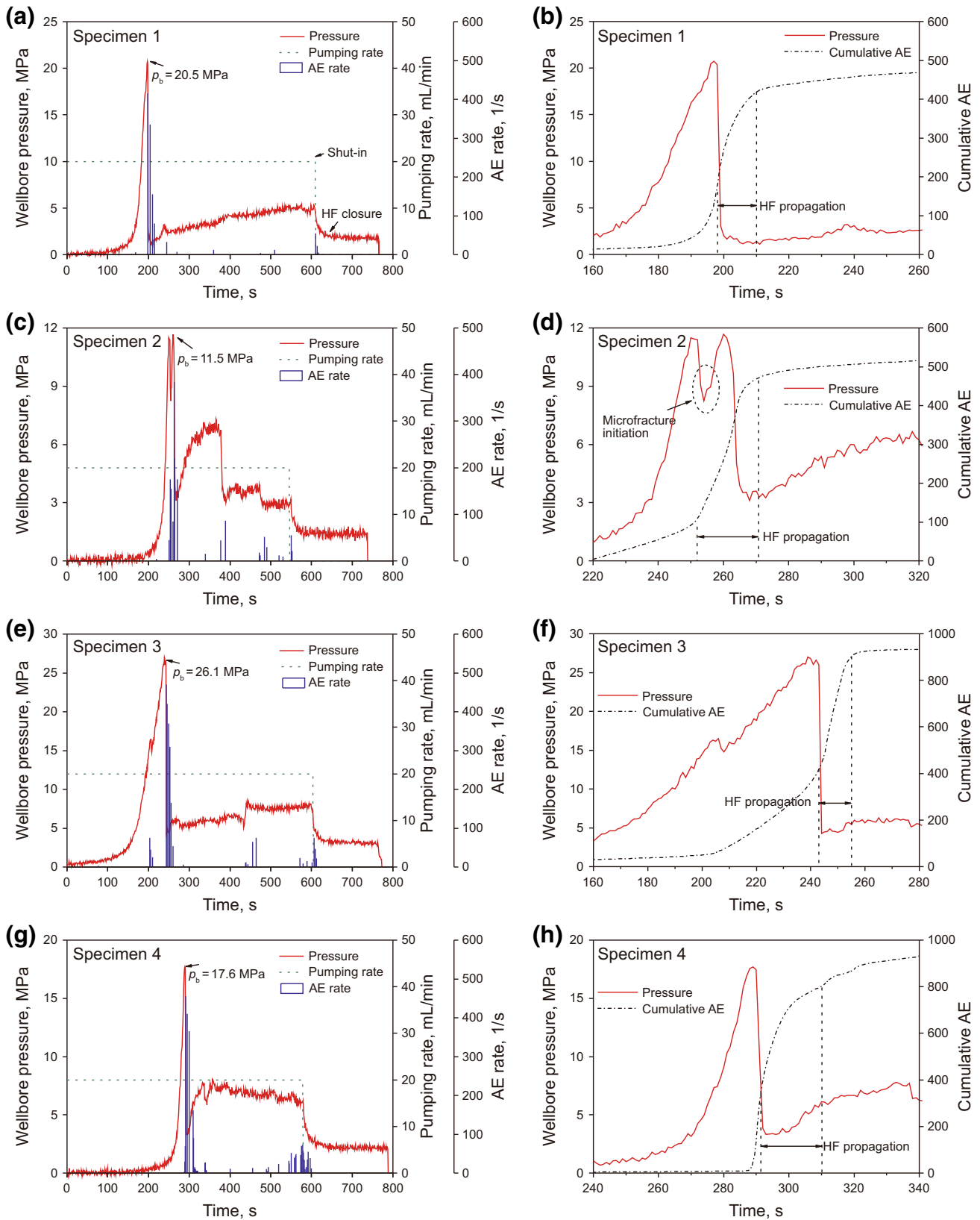


**Fig. 5** Wellbore pressure (red line), pumping rate (green dashed line), AE rate (blue rectangle), and cumulative AE (black dash dotted line) as a function of time for four specimens. The figures on the left (**a**, **c**,

**e**, and **g**) show the results during the entire experiments; the figures on the right (**b**, **d**, **f**, and **h**) present the results obtained during the several seconds before and after breakdown

**Table 4** Summary of experimental results

No.	Breakdown pressure, MPa	Pressure buildup interval, s	Pressure buildup rate, MPa/s	Pressure decline interval, s	Pressure decline rate, MPa/s	Max AE rate, 1/s	Fracture geometry
1	20.5	177–198	0.7	198–200	– 6.2	415	A single HF traversing the horizontal wellbore
2	11.5	239–250	0.8	260–266	– 1.6	384	A single HF obliquely traversing the horizontal wellbore
3	26.1	170–238	0.3	240–244	– 4.4	470	A complex HF traversing the horizontal wellbore
4	17.6	270–287	0.9	289–292	– 4.6	456	A complex HF aligning with the horizontal wellbore

**Table 5** Classification of focal mechanisms in conglomerate specimens

No.	Period, s	Cumulative AE	Compressive, %	Tensile, %	Shear, %
1	198–210	425	4.6	62.1	33.3
2	253–271	503	5.3	51.3	43.4
3	244–255	915	4.9	42.0	53.1
4	291–310	800	3.4	34.8	61.8

The failure mode/hypocenter mechanism of the AE events was determined statistically by analyzing the polarities of the P-wave first motions and the ratios ( $\lambda$ ) of dilation first motions to the total number of first motions (Lei et al. 1992, 2001; Bennour et al. 2015; Li et al. 2018a, b). Lei et al. (1992) set the intervals  $\lambda < 0.3$ ,  $0.3 \leq \lambda \leq 0.7$ , and  $\lambda > 0.7$  to determine tensile, shear, and compressive events, respectively. Only the data received by more than 10 AE sensors were used to achieve good reliability. The HF growth geometries on the specimen surfaces after the experiments were observed directly based on tracer distributions. Then, CT scanning was performed to reveal the internal HF geometry. Specimens 1 and 2 were scanned only once above the wellbore, and one CT image was obtained based on the simple HF geometry observed. Specimens 3 and 4 were scanned more than once in different directions, and five CT images were obtained based on the observed complex HF geometry. Finally, the specimens were split to reveal the HF growth paths inside and to verify the reliability of the CT images based on the tracer distributions. Table 3 summarizes the parameters used in the fracturing experiments.

### 3 Results and analysis

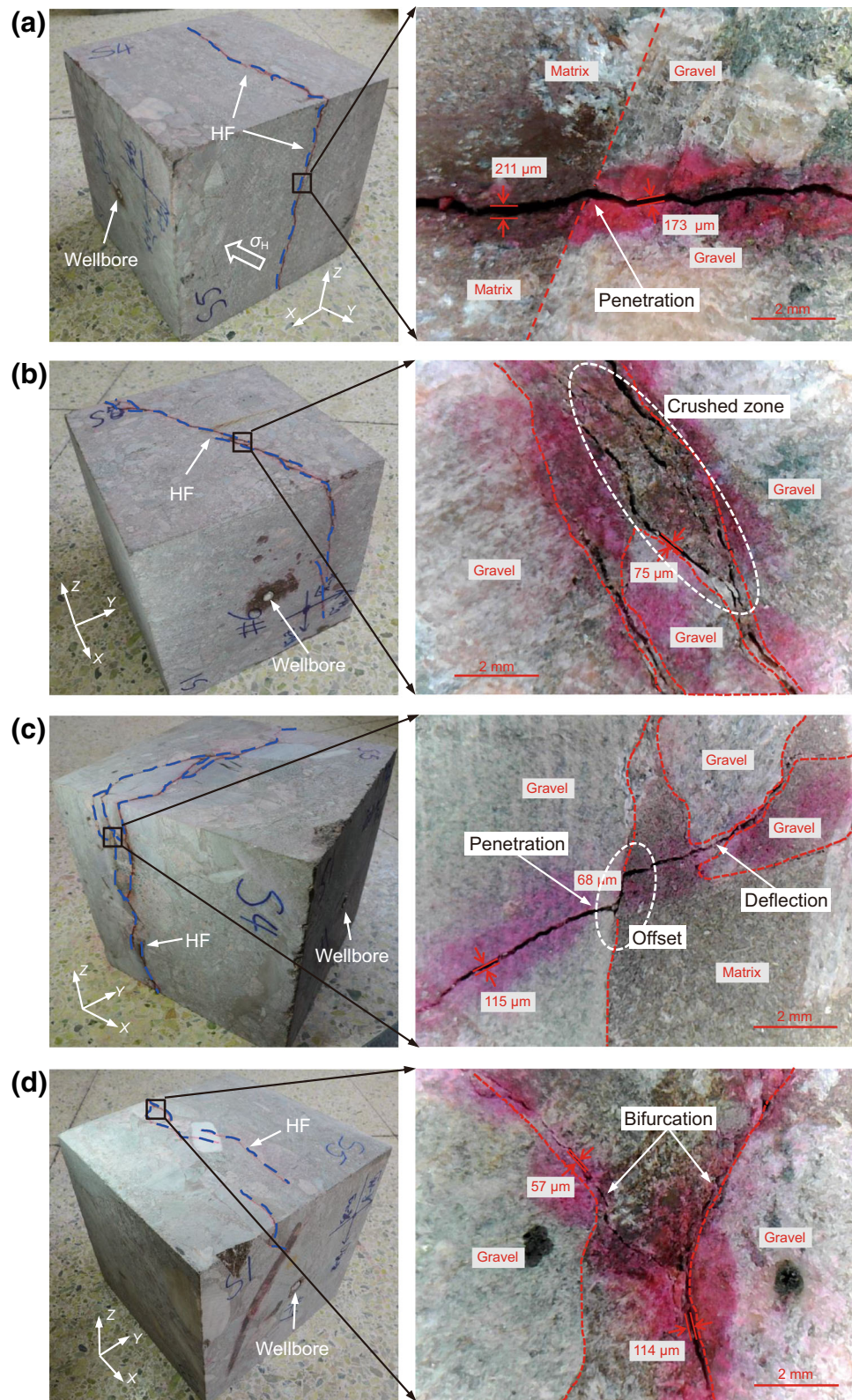
#### 3.1 Wellbore pressure, AE rate, and cumulative AE curves

Figure 5 illustrates the curves of wellbore pressure, AE rate, and cumulative AE events versus injection time for the four experiments. Tables 4 and 5 summarize the

experimental results (pressure buildup and decline rates were calculated during the tens of seconds before and after HF initiation) and the classification of focal mechanisms (including tensile, shear, and compressive), respectively. Wellbore pressure increased gradually as the fracturing fluid was injected into the wellbore. Once a HF was initiated from the open hole, the pressure decreased sharply from a peak value, namely the breakdown pressure ( $p_b$ ). Subsequently, the HF continued to propagate until the specimen boundaries were reached. AE events occurred in a concentrated fashion in the tens of seconds before and after HF initiation at the breakdown pressure. Then, the AE events occurred sporadically while the pressure fluctuated remarkably. The events coinciding with shutting down of the syringe pump may have resulted from the shearing of asperities on the fracture surfaces. HF initiation and propagation, tortuosity of the HF growth paths, and HF width within the conglomerate specimens were well reflected by the curves. The findings will be discussed in detail in the following sections.

#### 3.2 Fracture growth in conglomerate containing small gravels

Specimens 1 and 2 contained numerous relatively small gravel particles (considerably smaller in size than the specimens) with favorable sorting (Table 1), and they were hydraulically fractured under two horizontal differential stresses ( $\sigma_H - \sigma_h$ ). A single HF traversing the horizontal wellbore was created in Specimen 1, which was subjected to a relatively high horizontal differential stress  $\sigma_H - \sigma_h = 10$  MPa, as displayed in Fig. 6a. Overall, the resulting HF



**Fig. 6** HF growth paths on the specimen surfaces. **a** Transverse HF with relatively straight path and large width in Specimen 1. **b** Obliquely transverse HF with locally crushed zone and small width in Specimen 2. **c** Multiple tortuous HF traversing the wellbore

in Specimen 3. **d** HF's diversion into multiple interfaces between the matrix and large gravel particles aligning with the wellbore in Specimen 4. The red dashed line is the gravel boundary

in Specimen 1 was aligned with the direction of maximum horizontal stress ( $\sigma_H$ ), and it penetrated most of the small gravel particles, resulting in a relatively straight HF path with a large width. In this case, an increase in pressure buildup rate was approximately 0.7 MPa/s until the breakdown pressure of 20.5 MPa was reached (Fig. 5a).

**Fig. 9** CT image of HF growth path and AE source distributions for Specimen 3. **a** CT scan position indicator. **b** CT1 at  $Y = -3$  cm. **c** CT2 at  $Y = 5$  cm. **d** CT3 at  $Y = -12$  cm. **e** CT4 at  $Z = -5$  cm. **f** CT5 at  $Z = 5.5$  cm

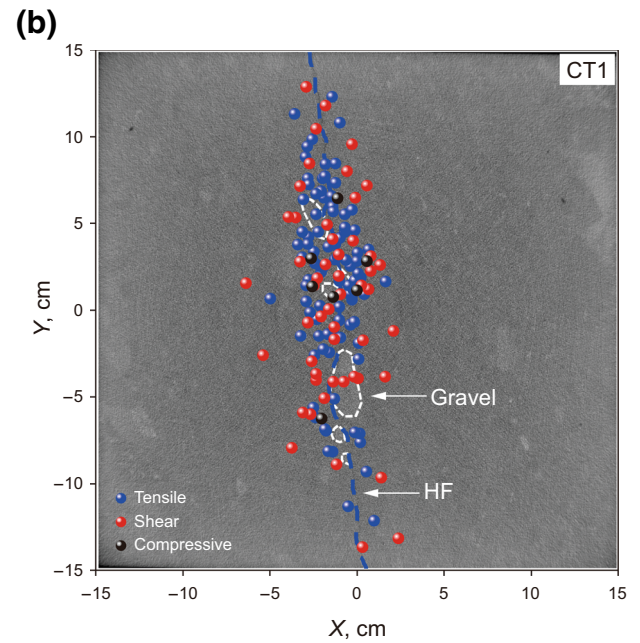
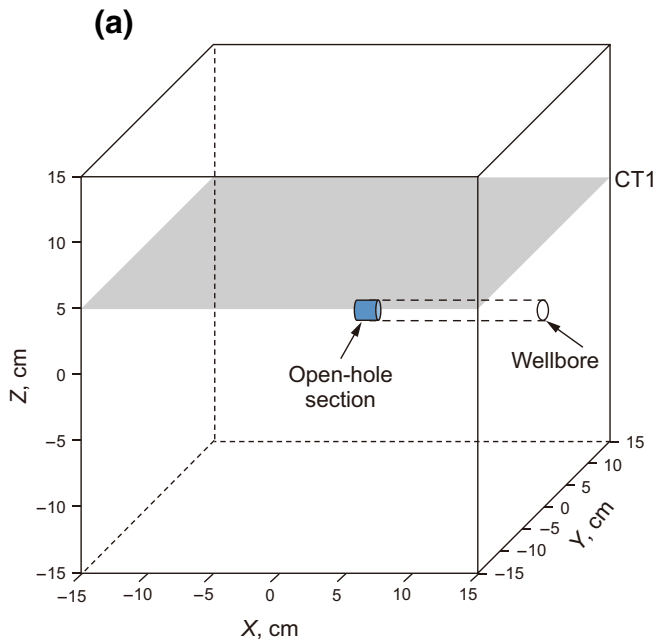


**Fig. 7** CT image of HF growth path and AE source distributions for Specimen 1. **a** CT scan position indicator. **b** CT1 at  $Z = 5$  cm. Only several relatively large gravels were marked in the CT images, and

the blue, red, and black balls represent the tensile, shear, and compressive events, respectively (the same as in the following figures)

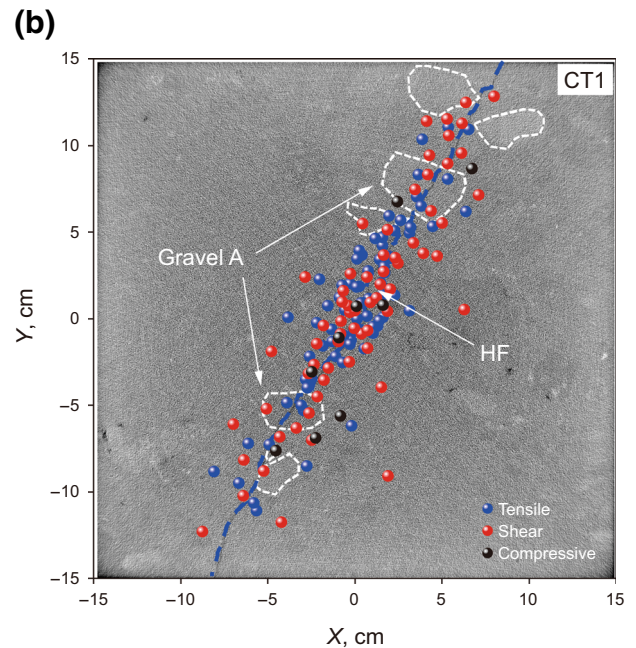
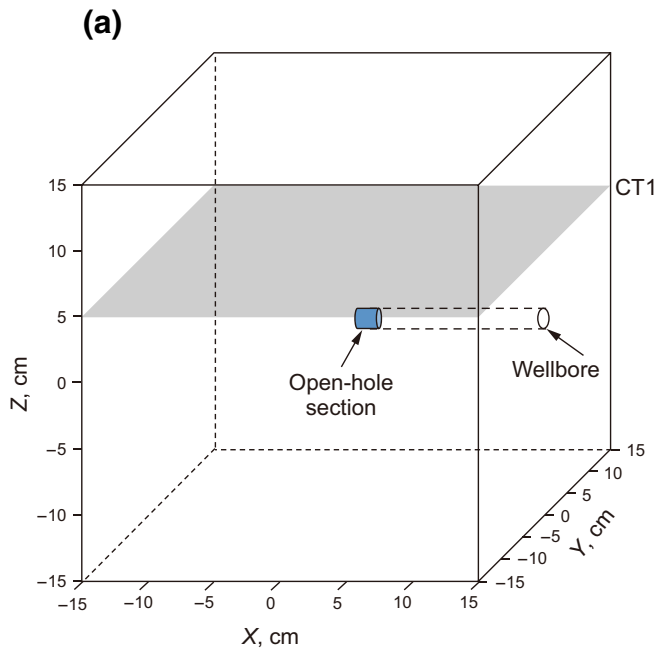
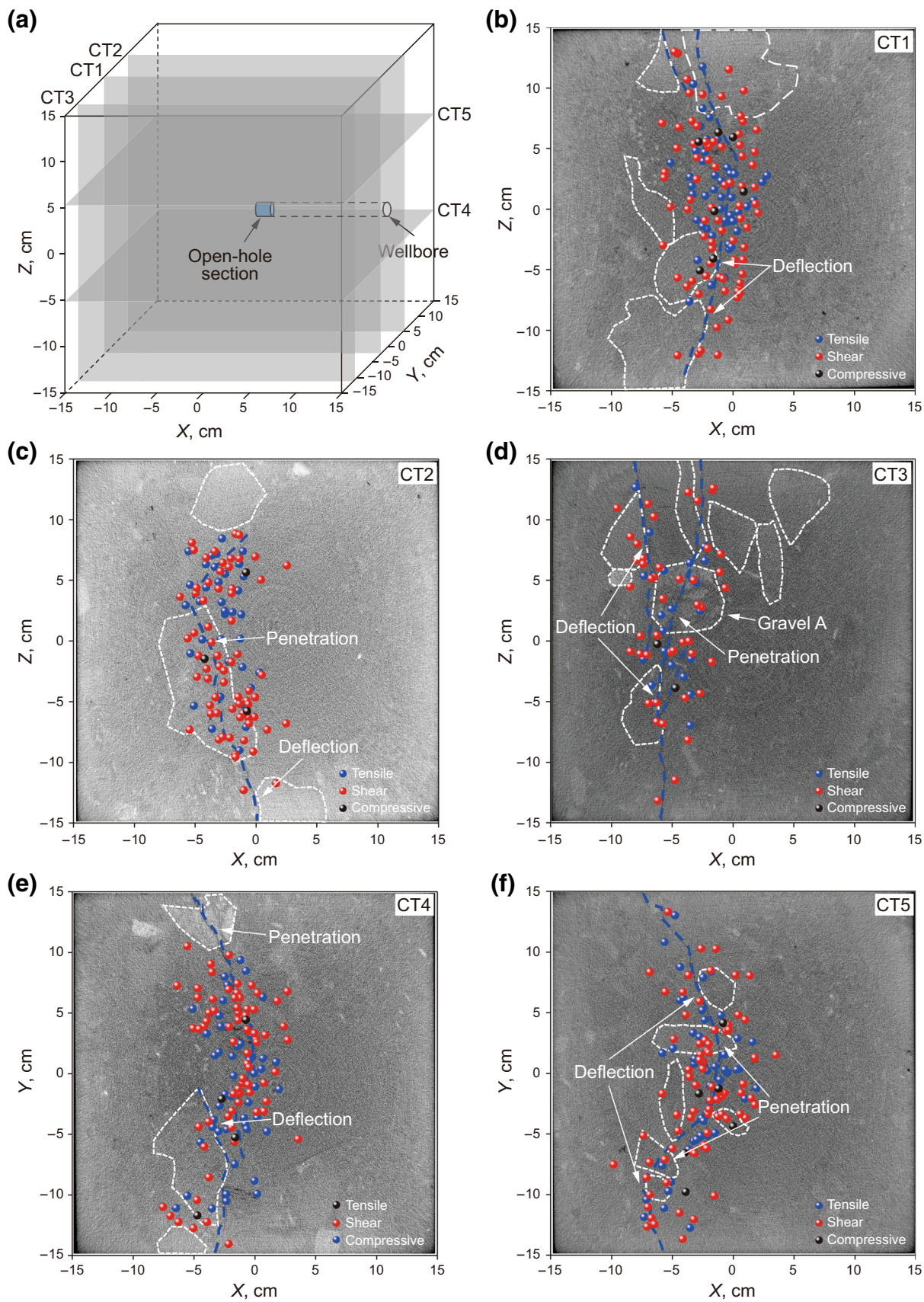


**Fig. 8** CT image of HF growth path and AE source distributions for Specimen 2. **a** CT scanning position indicator. **b** CT1 at  $Z = 5$  cm





After breakdown, the pressure declined initially at a rate of  $-6.2$  MPa/s. A maximum AE rate of  $415$  1/s was presented at the injection time of  $198$  s, thereby indicating HF initiation. A total of  $425$  effective AE events were recorded from  $198$  to  $210$  s, thereby indicating HF propagation (Fig. 5b). Then, the number of cumulative AE events increased slightly; this phenomenon corresponded only to the fluid penetration into the opened HF. Furthermore, HF growth behavior inside Specimen 1 could be observed clearly and analyzed from the CT images and AE source distributions (Fig. 7). In Fig. 7b, a narrowly focused distribution of AE events (ball) that traces a simple HF (blue dashed line) can be observed. This distribution confirms that the AE technique was successfully applied to monitor the fracturing process in the specimens used in this study. Moreover, the analysis of the focal mechanisms indicated that the tensile mechanism (approximately  $62.1\%$ ) was dominant in Specimen 1, which is consistent with the formation of a simple HF oriented along the  $\sigma_H$  direction (Hampton et al. 2013).

Specimen 2 was subjected to isotropic horizontal stresses ( $\sigma_H - \sigma_h = 0$  MPa), wherein the HF was initiated obliquely across the horizontal wellbore, as shown in Fig. 6b. A considerable number of crushed zones consisting of microfractures developed in the area surrounding the HF. This phenomenon can be ascribed to the likely deflection of the HF into the numerous interfaces between the matrix and small gravels under isotropic horizontal stresses. In fact, even the quartz and feldspar grains can lead to the formation of complex branching and intergranular fractures owing to the tendency of the HF to grow along the grain boundaries (Matsunaga et al. 1993). Consequently, the fracture width was smaller in Specimen 2 than that in Specimen 1. This was well reflected by a low pressure decline rate of  $-1.6$  MPa/s after the breakdown (Table 4). In Specimen 2, the HF was initiated from a gravel particle (Gravel-A) with a strength lower than that of the conglomerate matrix and even the interface (Table 2); thus, a lower breakdown pressure of  $11.5$  MPa was observed compared to that of Specimen 1 (Fig. 5c, d). Correspondingly, the maximum AE rate ( $384$  1/s) that indicates the breakdown pressure was low as well. The number of AE events recorded ( $503$ ) was larger in Specimen 2 than that in Specimen 1 because many microfractures were created in Specimen 2 during HF propagation ( $253$ – $271$  s). Meanwhile, the rates of tensile ( $51.3\%$ ) and shear ( $43.4\%$ ) events in the total events recorded are close to those in Specimen 2 (Table 5). The AE events recorded (Fig. 8) have a more diffuse distribution in Specimen 2 than in Specimen 1 (Fig. 7). The HF that penetrated through several mechanically weak gravel particles (Gravel-A) can be observed in the CT image of specimen 2 (Fig. 8b).

### 3.3 Fracture growth in conglomerate containing large gravels

Specimens 3 and 4 contained numerous relatively large gravel particles (similar in size to the specimens) with poor sorting (Table 2). In both specimens, the resulting HF geometries were more complex than those created in Specimens 1 and 2. In Specimens 3 and 4, the HF growth paths could be reoriented and bifurcated owing to the presence of large gravel particles.  $\sigma_H - \sigma_h = 10$  MPa was applied to Specimen 3 as applied to Specimen 1. The overall HF growth paths in Specimen 3 were perpendicular to the wellbore and were aligned with the direction of  $\sigma_H$ , as shown in Fig. 6c. In this case, the HF penetrated through the gravel particles and deflected into the interfaces. Specimen 4 was subjected to  $\sigma_H - \sigma_h = 0$  MPa, the same as Specimen 2, and in this specimen, nearly all HFs are deflected into the interfaces and aligned with the wellbore, as depicted in Figs. 6d. This phenomenon was mainly attributed to the distribution and arrangement of large gravel particles along the wellbore in Specimen 4. The fracture widths of Specimens 3 and 4 were similar to each other and smaller than that in Specimen 1, but they were larger than that in Specimen 2 (Fig. 6). This was consistent with the moderate post-breakdown pressure decline rates of  $-4.4$  and  $-4.6$  MPa/s for Specimens 3 and 4, respectively (Table 4).

In Specimen 3, the HF was initiated from a gravel particle (Gravel-B) with strength higher than that of the conglomerate matrix. Thus, Specimen 3 exhibited the highest breakdown pressure of  $26.1$  MPa among the four specimens (Fig. 5c). Consequently, the maximum AE rate of  $470$  1/s and cumulative  $915$  AE events were the highest during HF initiation and propagation ( $244$ – $255$  s) in Specimen 3. Figure 9 presents CT images of the HF growth paths and AE source distributions in Specimen 3. Complex fracture growth paths within Specimen 3 were observed on the specimen surfaces. The propagation of a HF branch can be well defined based on located AE events. The HF likely propagated in the shear mode along the matrix/gravel interfaces. Thus, the percentage of shear events ( $53.1\%$ ) in Specimen 3 was higher than that of tensile events ( $42\%$ ) (Table 5).

In Specimen 4, the HF was initiated at a breakdown pressure of  $17.6$  MPa (Fig. 5d) and was indicated by a maximum AE rate of  $456$  1/s (Table 4). A total of  $800$  AE events were recorded during HF propagation ( $291$ – $391$  s). Figure 10 illustrates the CT images of HF growth paths and AE source distributions in Specimen 4. Multiple HF branches were created and were well traced by the AE source distributions. Major AE activity was concentrated around the open hole (Fig. 10b). In this case, most HF

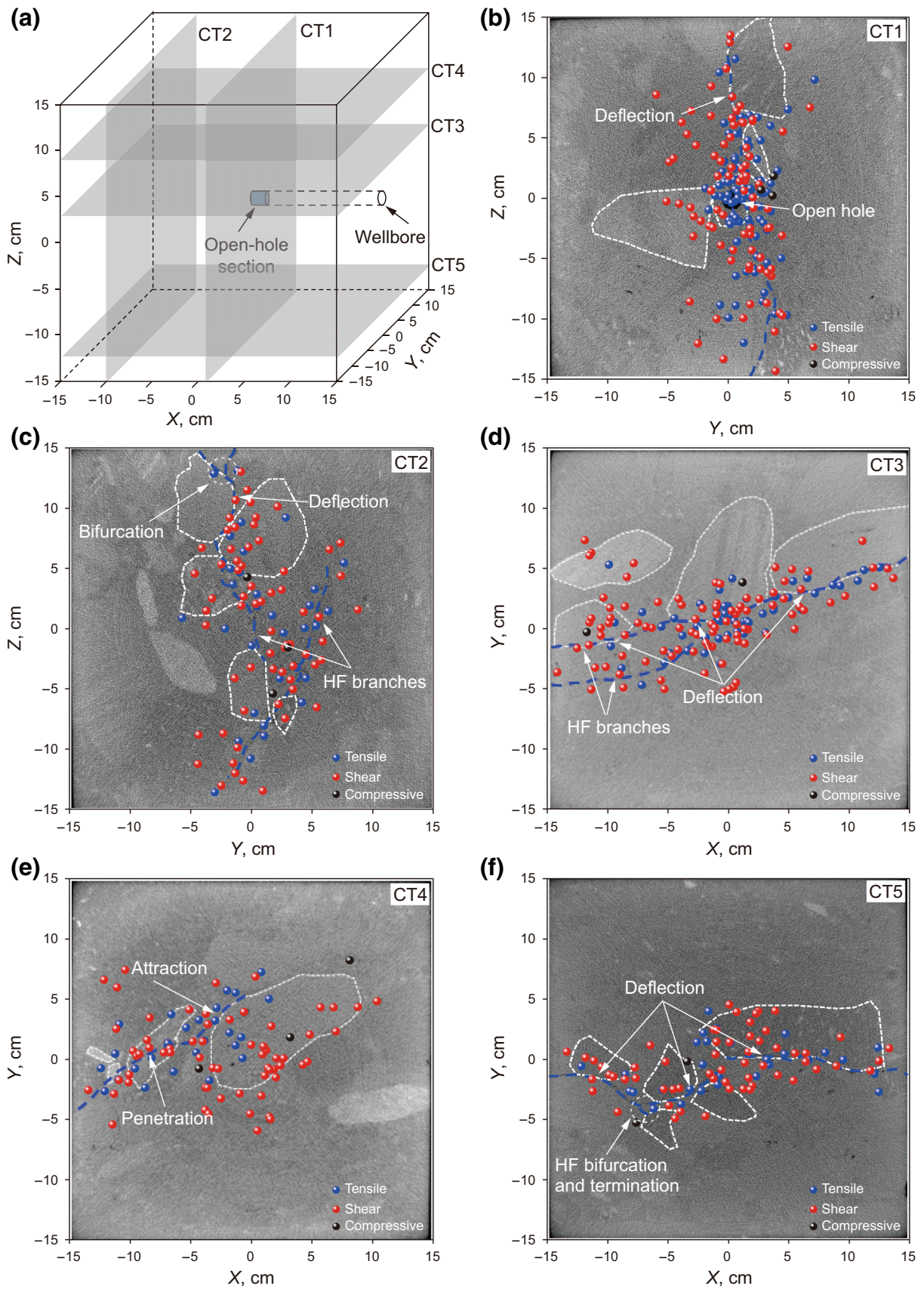


**Fig. 10** CT image of HF growth path and AE source distributions for Specimen 4. **a** CT scan position indicator. **b** CT1 at  $X = 0.8$  cm. **c** CT2 at  $X = -10$  cm. **d** CT3 at  $Z = 3$  cm. **e** CT4 at  $Z = 8.8$  cm. **f** CT5 at  $Z = -12.2$  cm

branches in Specimen 4 propagated along the matrix/gravel interfaces; therefore, the shear mechanism was predominant. The AE event density was high around the matrix/gravel interface. The percentage of shear events was 61.8% in Specimen 4. This tendency is consistent with the report that HF propagation within a pre-existing plane is based preliminarily on shear failure (Talebi and Cornet 1987; Molenda et al. 2015).

## 4 Discussion and conclusions

In the present study, HF growth behavior and AE response features of conglomerate specimens were determined by conducting fracturing experiments in the laboratory combined with CT scanning and AE monitoring. We found obvious differences in terms of breakdown pressure, HF complexity, and focal mechanism of AE events between conglomerate specimens containing gravels of various sizes and mechanical strengths. The HF growth geometry was influenced strongly by the lithological heterogeneity associated with the presence of gravels in conglomerate. Simple and planar HF was likely created in conglomerate when gravels were considerably smaller than the specimens even under the isotropic horizontal stress condition (0 MPa), whereas multiple HF branches with tortuous paths were created along the matrix/gravel interfaces, thereby resulting in a complex geometry, in conglomerate when the gravels were similar in size to the specimens, even under a high horizontal differential stress (10 MPa). Fracture complexity was found to be dependent on the distributions and arrangement of large gravel particles. Pressure and AE rate curves well reflected HF initiation and propagation, as well as the tortuosity and width of a HF. Breakdown pressure and AE rate would be higher when a HF was initiated from a mechanically strong gravel compared with the case in the conglomerate matrix. A large pressure decline rate after breakdown indicated the generation of a planar and wide fracture. By contrast, a small pressure decline rate after breakdown corresponded to the creation of narrow fractures. Tensile events occurred during HF initiation and were concentrated around the wellbore. The tensile mechanism was dominant when a simple and planar HF was created. The shear mechanism became generally dominant with increasing HF complexity. Shear events occurred mainly around the nonplanar and complex matrix/gravel interfaces.

However, there still exists some limitation in the translation of these experimental results to field application. For instance, the creation of complex HFs at the laboratory scale may be attributed to the fact that the dominant gravel particles in Specimens 3 and 4 were similar in size to the specimens or HFs, as shown in Table 1. At the field scale, the gravel particles are generally considerably smaller than the HF. Thus, it is unreasonable to directly translate these results for predicting field-scale HFs. A systematic experimental simulation should be performed to better understand the separation of gravel sizes for simple and complex HFs.

**Acknowledgements** This paper was supported by the Major National Science and Technology Projects of China (No. 2016ZX05046004-002; No. 2017ZX05039002-003), and the National Basic Research Program of China (No. 2015CB250903).

**Open Access** This article is distributed under the terms of the Creative Commons Attribution 4.0 International License (<http://creativecommons.org/licenses/by/4.0/>), which permits unrestricted use, distribution, and reproduction in any medium, provided you give appropriate credit to the original author(s) and the source, provide a link to the Creative Commons license, and indicate if changes were made.

## References

- Bennour Z, Ishida T, Nagaya Y, Chen Y, Nara Y, Chen Q, et al. Crack extension in hydraulic fracturing of shale cores using viscous oil, water, and liquid carbon dioxide. *Rock Mech Rock Eng.* 2015;48:1463–73. <https://doi.org/10.1007/s00603-015-0774-2>.
- Frash L, Gutierrez M, Hampton J. Scale model simulation of hydraulic fracturing for EGS reservoir creation using a heated true-triaxial apparatus. In: ISRM international conference for effective and sustainable hydraulic fracturing. International Society for Rock Mechanics; 2013.
- Hampton J, Frash L, Gutierrez M. Investigation of laboratory hydraulic fracture source mechanisms using acoustic emission. In: 47th U.S. rock mechanics/geomechanics symposium. American Rock Mechanics Association; 2013.
- Hu X, Wu K, Song X, Yu W, Tang J, Li G, et al. A new model for simulating particle transport in a low-viscosity fluid for fluid-driven fracturing. *AIChE J.* 2018a. <https://doi.org/10.1002/aic.16183>.
- Hu X, Wu K, Li G, Tang J, Shen Z. Effect of proppant addition schedule on the proppant distribution in a straight fracture for slickwater treatment. *J Pet Sci Eng.* 2018b;167:110–9. <https://doi.org/10.1016/j.petrol.2018.03.081>.
- Ju Y, Yang Y, Chen J, Liu P, Dai T, Guo Y, et al. 3D reconstruction of low-permeability heterogeneous glutenites and numerical simulation of hydraulic fracturing behavior. *Chin Sci Bull.* 2016a;61:82–93.
- Ju Y, Liu P, Chen JL, Yang YM, Ranjith PG. CDEM-based analysis of the 3D initiation and propagation of hydrofracturing cracks in heterogeneous glutenites. *J Nat Gas Sci Eng.* 2016b;35:614–23. <https://doi.org/10.1016/j.jngse.2016.09.011>.
- Lei XL, Nishizawa O, Kusunose K, Satoh T. Fractal structure of the hypocenter distributions and focal mechanism solutions of acoustic emission in two granites of different grain sizes.

- J Phys Earth. 1992;40(6):617–34. <https://doi.org/10.4294/jpe1952.40.617>.
- Lei XL, Kusunose K, Rao MVMS, Nishizawa O, Satoh T. Quasi-static fault growth and cracking in homogeneous brittle rock under triaxial compression using acoustic emission monitoring. *J Geophys Res*. 2001;105(B3):6127–39. <https://doi.org/10.1029/1999JB900385>.
- Li LC, Li G, Meng QM, Wang H, Wang Z. Numerical simulation of propagation of hydraulic fractures in glutenite formation. *Chin J Rock Soil Mech*. 2013;34(5):1501–7.
- Li N, Zhang SC, Zou YS, Ma XF, Wu S, Zhang YN. Experimental analysis of hydraulic fracture growth and acoustic emission response in a layered formation. *Rock Mech Rock Eng*. 2018a;51(4):1047–62. <https://doi.org/10.1007/s00603-017-1383-z>.
- Li N, Zhang SC, Zou YS, Ma XF, Zhang ZP, Li SH, et al. Acoustic emission response of laboratory hydraulic fracturing in layered shale. *Rock Mech Rock Eng*. 2018b; 51(11):3394–406. <https://doi.org/10.1007/s00603-018-1547-5>.
- Lockner D, Byerlee JD. Hydrofracture in Weber sandstone at high confining pressure and differential stress. *J Geophys Res Atmos*. 1977;82(14):2018–26. <https://doi.org/10.1029/JB082i014p02018>.
- Ma XF, Zou YS, Li N, Chen M, Zhang YN, Liu ZZ. Experimental study on the mechanism of hydraulic fracture growth in a glutenite reservoir. *J Struct Geol*. 2017;97:37–47. <https://doi.org/10.1016/j.jsg.2017.02.012>.
- Matsunaga I, Kobayashi H, Sasaki S, Ishida T. Studying hydraulic fracturing mechanism by laboratory experiments with acoustic emission monitoring. *Intern J Rock Mech Min Sci Geomech Abstr*. 1993;30(7):909–12. [https://doi.org/10.1016/0148-9062\(93\)90043-D](https://doi.org/10.1016/0148-9062(93)90043-D).
- Meng QM, Zhang SC, Guo XM, Chen XH, Zhang Y. A primary investigation on propagation mechanism for hydraulic fractures in glutenite formation. *J Oil Gas Technol*. 2010;32(4):119–23.
- Mogi K. Earthquakes and fractures. *Tectonophysics*. 1967;5(1):35–55. [https://doi.org/10.1016/0040-1951\(67\)90043-1](https://doi.org/10.1016/0040-1951(67)90043-1).
- Molenda M, Stockhert F, Brenne S, Alber M. Acoustic emission monitoring of laboratory scale hydraulic fracturing experiments. In: 49th US rock mechanics/geomechanics symposium. American Rock Mechanics Association; 2015.
- Stanchits S, Vinciguerra S, Dresen G. Ultrasonic velocities, acoustic emission characteristics and crack damage of basalt and granite. *Pure appl Geophys*. 2006;163(5):975–94. <https://doi.org/10.1007/s00024-006-0059-5>.
- Stanchits S, Surdi A, Edelman E, Suarez-Rivera R. Acoustic emission and ultrasonic transmission monitoring of hydraulic fracture propagation in heterogeneous rock samples. In: 46th US rock mechanics/geomechanics symposium. American Rock Mechanics Association; 2012.
- Stanchits S, Burghardt J, Surdi A. Hydraulic fracturing of heterogeneous rock monitored by acoustic emission. *Rock Mech Rock Eng*. 2015;48(6):2513–27. <https://doi.org/10.1007/s00603-015-0848-1>.
- Talebi S, Cornet FH. Analysis of microseismicity induced by a fluid injection in a granite rock mass. *Geophys Res Lett*. 1987;14:227–30. <https://doi.org/10.1029/GL014i003p00227>.
- Tang J, Wu K, Zeng B, Huang H, Hu X, Guo X, et al. Investigate effects of weak bedding interfaces on fracture geometry in unconventional reservoirs. *J Petrol Sci Eng*. 2018a;165:992–1009. <https://doi.org/10.1016/j.petrol.2017.11.037>.
- Tang J, Wu K, Li Y, Hu X, Liu Q, Ehlig-Economides C. Numerical investigation of the Interactions between hydraulic fracture and bedding planes with non-orthogonal approach angle. *Eng Frac Mech*. 2018b;200:1–16. <https://doi.org/10.1016/j.engfracmech.2018.07.010>.
- Yashwanth C, Camilo M, Carl S, Chandra R. An experimental investigation into hydraulic fracture propagation under different applied stresses in tight sands using acoustic emissions. *J Pet Sci Eng*. 2013;108:151–61. <https://doi.org/10.1016/j.petrol.2013.01.002>.
- Zoback MD, Rummel F, Jung R, Raleigh CB. Laboratory hydraulic fracturing experiments in intact and pre-fractured rock. *Int J Rock Mech Min Sci Geophys Abstr*. 1977;14(2):49–58. [https://doi.org/10.1016/0148-9062\(77\)90196-6](https://doi.org/10.1016/0148-9062(77)90196-6).
- Zou YS, Zhang SC, Zhou T, Zhou X, Guo TK. Experimental investigation into hydraulic fracture network propagation in gas shales using CT scanning technology. *Rock Mech Rock Eng*. 2016;49:33–45. <https://doi.org/10.1007/s00603-015-0720-3>.
- Zou YS, Ma XF, Zhou T, Li N, Chen M, Li SH, et al. Hydraulic fracture growth in a layered formation based on fracturing experiments and discrete element modeling. *Rock Mech Rock Eng*. 2017;50:2381–95. <https://doi.org/10.1007/s00603-017-1241-z>.